Strain-Modulated Perfect Valley Precession and Valley Transistor in Graphene

Ruigang Li,[1] Jun-Feng Liu,[1,*] and Jun Wang[2,†]
[1] *School of Physics and Materials Science, Guangzhou University, Guangzhou 510006, China*
[2] *Department of Physics, Southeast University, Nanjing 210096, China*

(Received 10 November 2022; revised 6 January 2023; accepted 1 February 2023; published 28 February 2023)

We propose the realization of perfect valley precession by use of strain, which gives rise to an effective vector potential and moves two valleys in opposite directions in momentum space. It is shown that the spatial precession period is independent of both the Fermi energy and the transverse wave vector. This is crucial to perfect precession in a practical device with multiple transverse wave vectors or modes. To theoretically demonstrate the perfect valley precession, we investigate the conductivity of a Kekulé graphene superlattice/graphene/Kekulé graphene superlattice junction that acts as a valley transistor. Due to the valley precession, the conductivity exhibits perfect oscillations with the strain and the conductivity minima are very close to zero. Our finding provides a strategy to design ideal valleytronics and straintronics devices.

DOI: 10.1103/PhysRevApplied.19.024075

I. INTRODUCTION

Since graphene (GR) [1–4] was successfully isolated, it has become a candidate material to design valleytronics devices [5–8]. The K and K' valleys of graphene are well separated in reciprocal space. In the absence of short-range defects or disorders, the valleys can be treated as independent as the intervalley scattering is suppressed. The valley-related properties and applications of graphene have been widely studied, such as the valley Hall [9–13] or anomalous Hall effect [14,15] , valley caloritronics [16–19], valley filter effect [20–23], valley transistors [24–27], etc.

A main challenge in developing valleytronics devices is how to manipulate the valley degree of freedom effectively. Recently, Kekulé-patterned graphene superlattices (KGSs) [28–33] were proposed and provided a valley engineering mechanism. In these superlattices, two valleys of pristine graphene are folded into the Γ point of the Brillouin zone, coupled by Bragg scattering [31,34,35]. Especially, Kekulé-Y-patterned graphene (KYG) has been found in the laboratory by growing graphene on a Cu(111) substrate, with the copper atoms adsorbed on the graphene lattices [30].

Valley precession is one of the key aims of valley manipulation [24,36–40]. Similar to spin precession in a Datta-Das spin field effect transistor due to Rashba spin-orbit interaction [41], the valley-coupled interaction in a KGS can precess the valley in real space [38]. Thus, KGS/GR hybrid junctions were proposed to design valley precession devices [38–40]. Wang *et al.* examined the valley precession in GR/KGS/GR junctions based on a continuum model. The valley of the incident electron is rotated by the valley-coupled interaction in the KGS region [38]. Valley precession is also found in GR/KYG/GR junctions based on a tight-binding (TB) model [39]. In the TB model, the C—C bonds, formed by the adsorbed atom and its nearest-neighbor atoms, were shortened [30]. Wu *et al.* studied the valley precession and valley polarization in GR/KYG/GR junctions. They point out that high valley polarization with large valley-polarized currents can be obtained by the use of strain [40].

However, there are two main shortcomings in these valley precession junctions. First, the valley precession rates of modes with different transverse momenta are not the same and the conductivity cannot be completely suppressed in a practical device with multiple transverse modes. Second, the valley precession rate is hard to tune and the precession length cannot be changed once the junction is built. These problems are not easy to overcome in the above GR/KGS/GR junctions.

In graphene, strain can also be used to manipulate the valley degree of freedom. Pereira and Castro Neto [42] and Zhai *et al.* [43] pointed out that strain would introduce a pseudovector potential to valley K, with its sign reversed for valley K' for conserving time-reversal symmetry. Valleys K and K' are shifted in opposite directions in reciprocal space. It is worth noting that, under a first-order approximation, the uniaxial strain and shear strain (no matter along zigzag or armchair directions) can separate the valleys along armchair and

---

[*] phjfliu@gzhu.edu.cn
[†] jwang@seu.edu.cn

zigzag directions in reciprocal space, respectively [44–46].

In this work, we propose a perfect valley precession in KYG/GR/KYG junctions where the precession is modulated by a strain applied in the central GR region. The incident electrons from the KYG lead to valley K-K' precessing in the strained graphene region due to the separation of two folded valleys K and K' in momentum space induced by the strain [see Figs. 1(d)–1(f)]. The precession rate, determined only by the strain, is independent of both the incident energy and the transverse momentum of the incident electrons. Therefore, the conductivity exhibits perfect oscillations with the strain, and the conductivity minima are very close to zero. We theoretically demonstrate a perfect valley precession and a valley transistor behavior in KYG/GR/KGR junctions based on both analytic discussion and numerical calculation. The numerical calculation is carried out using Kwant [47] based on the tight-binding model and the lattice Green's function technique.

II. MODEL

Figure 1(c) sketches the junction that we study. The central graphene is connected to two Kekulé-Y-patterned graphene leads along the x direction. We assume the transport is along the zigzag direction. The uniaxial strain can be applied to the central graphene region to separate the two folded valleys in the k_x direction. The primitive vectors of KYG are $a_1 = 3(\sqrt{3}, 1)a/2$ and $a_2 = 3(\sqrt{3}, -1)a/2$, where $a = 1.42$ Å denotes the length of C—C bonds of the graphene lattice [1,3]. Two valleys K and K' are folded into the Γ point, shown in Fig. 1(b) [34,35]. We set the adsorption sites belonging to sites A by default, and sites B and C denote the nearest and next-nearest sites of sites A, respectively, as illustrated in Fig. 1(a). Due to the adsorption, the on-site energies will be altered for all sites. Normally, the adsorption will also shorten the A—B bond [30], altering the hopping energy of A—B bonds. The TB Hamiltonian of KYG reads [33]

$$H_{\mathrm{KYG}} = -\sum_{\langle ij\rangle}\left(t_M a_i^\dagger b_j + \mathrm{H.c.}\right) - \sum_{\langle ij\rangle}\left(t_0 b_i^\dagger c_j + \mathrm{H.c.}\right) + \sum_i \left(U_A a_i^\dagger a_i + U_B b_i^\dagger b_i + U_C c_i^\dagger c_i\right), \tag{1}$$

where $a_i^\dagger$ ($b_i^\dagger$, $c_i^\dagger$) is the creation operator of electrons at site A_i (B_i, C_i), $t_0 = 2.7$ eV is the nearest-neighbor hopping energy of pristine graphene, $t_M = t_0 + \delta t$ denotes the modified hopping energy between sites A and sites B, and U_A (U_B, U_C) is the on-site energy of sites A (B, C) introduced by the absorption. Note that U_C is small and set to zero in this study, i.e., $U_C = 0$.

As an example, we consider a simplified model of KYG by setting $U_B = 0$ and $\delta t = 0$. The low-energy continuum form of the Hamiltonian in Eq. (1) can be written as [33,38]

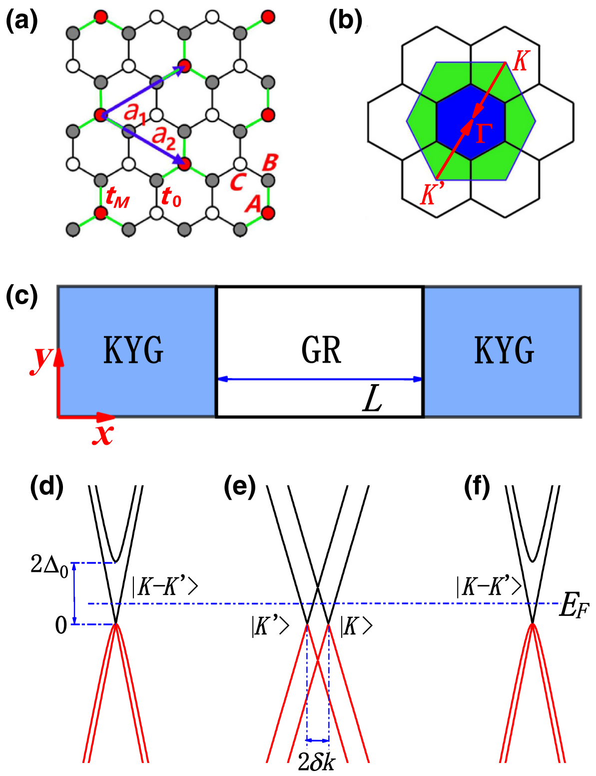

FIG. 1. (a) Schematic of the KYG lattice. (b) The first (blue) and the second (green) Brillouin zone of the KYG. The K and K' valleys are folded into the Γ point. (c) Schematic of the KYG/GR/KYG junction. The band structures of (d) the left KYG lead, (e) the central strained graphene, and (f) the right KYG lead. The transverse momentum is set to zero, i.e., $k_y = 0$. The valley-polarized electron with valley K-K' is injected into the scattering region with energy E_F, and the two folded valleys K and K' of graphene are separated along the transport direction by the strain, with distance $2\delta k$.

$$H_{\mathrm{KYG}} = v_{F0}\left(k_x\tau_0\sigma_x + k_y\tau_z\sigma_y\right) + \frac{\Delta_0}{2}\tau_0\left(\sigma_0 + \sigma_z\right) + \frac{\Delta_0}{2}\tau_x\left(\sigma_0 + \sigma_z\right), \tag{2}$$

where $\Delta_0 = U_A/3$, $v_{F0} = 3at_0/2$ is the Fermi velocity of electrons in graphene, and σ_α and τ_α ($\alpha = 0, x, y, z$) denote the Pauli matrices acting in the sublattice space and the valley space, respectively. The valley-coupled interaction comes from the last term of Eq. (2), which is only determined by U_A. The band structure $E_{\mathrm{KYG}}(k_x, k_y = 0)$ is shown in Figs. 1(d) and 1(f). Note that only the lowest conduction band (LCB) is occupied in the energy range $[0, 2\Delta_0]$, where the electron is valley polarized. In the following study, the Fermi energy is set to be in this range, which implies that both the incident and transmitted electrons are valley polarized in our KYG/GR/KYG junctions.

The low-energy continuum Hamiltonian of graphene can be recovered from Eq. (2) by setting $U_A = 0$. When a strain is applied, a valley-opposite pseudovector potential A_x is introduced effectively, which moves two valleys in opposite directions [42,43]. The corresponding low-energy Hamiltonian can be written as

$$H_{\mathrm{GR}} = v_{F0}\left[k_x\tau_0\sigma_x + A_x\tau_z\sigma_x + k_y\tau_z\sigma_y\right]. \tag{3}$$

The band structure $E_{\mathrm{GR}}(k_x, k_y = 0)$ is shown in Fig. 1(e). The distance between two valleys equals double the pseudovector potential, i.e., $2\delta k = 2A_x$.

When the Fermi energy E_F is fixed in the range $[0, 2\Delta_0]$, the wave function of incident electrons in the left KYG lead is given by

$$\Psi_{\mathrm{KYG}}(x,y) = \frac{1}{2}\left(\ 1, e^{i\phi}, -1, -e^{-i\phi}\ \right)^T e^{i(k_x x + k_y y)}, \tag{4}$$

where $\phi = \arcsin(v_{F0}k_y/E_F)$ is the incident angle of electrons. The corresponding dispersion of the LCB is $E(\boldsymbol{k}) = v_{F0}\sqrt{k_x^2 + k_y^2}$, which is exactly the same as the linear dispersion in graphene. From Eq. (4), it is seen that an incident electron is valley polarized to K-K'. Note that this K-K' valley-polarized state does not break the time-reversal symmetry, which is represented by the operator $T = \tau_x\sigma_z C$ [48] with C the complex conjugation operator, through the time-reversal exchange K and K'.

In the central graphene, the two valleys are decoupled, but split by the strain. The wave functions for valleys K and K' can be given by, respectively,

$$\Phi_K(x,y) = \frac{1}{\sqrt{2}}\left(\ 1, e^{i\phi}, 0, 0\ \right)^T e^{i[(k_x - \delta k)x + k_y y]}, \tag{5}$$

$$\Phi_{K'}(x,y) = \frac{1}{\sqrt{2}}\left(\ 0, 0, 1, e^{-i\phi}\ \right)^T e^{i[(k_x + \delta k)x + k_y y]}. \tag{6}$$

Note that the angle ϕ in the pseudospinor is the same as that in Eq. (4) due to the conservation of transverse momentum k_y and energy E_F. At the left KYG/GR interface $x = 0$, the incident wave function in KYG can be decomposed as $\Psi_i = [\Phi_K(0,y) - \Phi_{K'}(0,y)]/\sqrt{2}$. When this valley-polarized state propagates along the x direction in the central graphene, its valley is precessed due to δk. At the right GR/KYG interface $x = L$ with L the length of the central graphene region, the state becomes $\Psi_f = [\Phi_K(L,y) - \Phi_{K'}(L,y)]/\sqrt{2}$. Because the transmitted wave is the same as the incident wave, the transmission of this KYG/GR/KYG junction is approximately determined by the remaining component of initial state Ψ_i:

$$T(E_F, \phi) = |\langle\Psi_i|\Psi_f\rangle|^2 = \cos^2(\delta k L). \tag{7}$$

It is noticeable that the transmission is independent of both the Fermi energy and the incident angle, or the transverse momentum of electrons.

According to the Landauer formula, at a given Fermi energy E_F, the conductivity of the junction reads

$$\begin{aligned} G &= G_0\int_{-\pi/2}^{\pi/2} T(E_F;\phi)\,\cos\phi\, d\phi \\ &= 2G_0\cos^2(\delta k L), \end{aligned} \tag{8}$$

where $G_0 = (e^2/h)E_F/(\pi v_{F0})$ and the spin degree of freedom has been taken into account. For a given length L, the conductivity perfectly oscillates with δk, which is proportional to the applied strain [42,43].

Although the above discussion is based on the condition of $U_B = \delta t = 0$, the situation is similar in the case of $U_B \neq 0$ or $\delta t \neq 0$ if only the incident and transmitted electrons are valley polarized.

III. NUMERICAL RESULTS

In this section, we present the numerical results of conductivity of KYG/GR/KYG junctions along zigzag and armchair directions. The numerical calculation is carried out using Kwant [47] based on the tight-binding model and the lattice Green's function technique. First, we consider the simple case of $U_B = \delta t = 0$. Then we investigate the influence of nonzero U_B and δt.

A. $U_B = 0$ and $\delta t = 0$

First, we consider the simple case of $U_B = \delta t = 0$. For convenience, we refer to the junctions along the zigzag and the armchair directions as the zigzag junction (ZJ) and the armchair junction (AJ), respectively, as shown in Figs. 2(a) and 2(b). The x (y) direction is defined as the transport direction of ZJs (AJs), i.e., the zigzag (armchair) direction. The supercells of two leads and the scattering region are shown in Figs. 2(c) and 2(d). The size of both supercells is $a_Z \times a_A$, where $a_Z = 3\sqrt{3}a$ and $a_A = 3a$. The lengths of the scattering regions are $L_Z = N_Z a_Z$ for ZJ and $L_A = N_A a_A$ for AJ, where N_Z and N_A are the number of supercells along the transport directions. In both junctions, the translation symmetry is assumed to be preserved in the transverse direction and the transverse momentum, i.e., k_y for ZJs and k_x for AJs, is conserved in the transport. Thus, the two-dimensional junctions transform into quasi-one-dimensional junctions. The band structures of zigzag and armchair KYGs are the same, as shown in Figs. 1(d) and 1(f), with the transverse momenta set to zero.

When a strain is applied in the central graphene region, the hopping energy t_0 of pristine graphene will change to $t_0\exp[-\beta(d_\alpha/a - 1)]$ [49] with the strain applied, where $\beta = 3.37$ and $d_{\alpha=1,2,3}$ (a) is the bond length after (before) deformation as shown in Fig. 2(d). If a uniaxial strain is applied in the graphene region of ZJs along zigzag or armchair direction, the deformed bond lengths are,

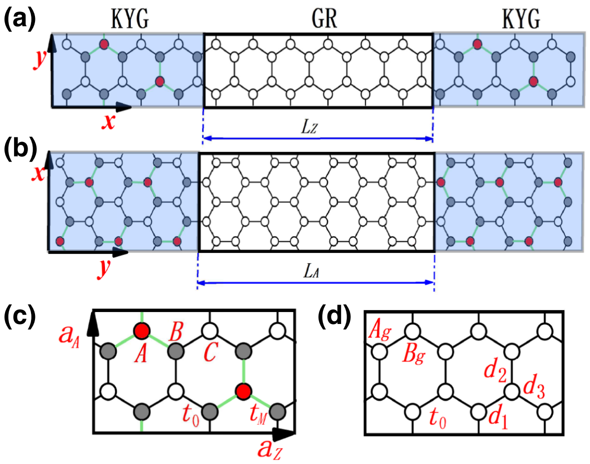

FIG. 2. Schematics of (a) the zigzag and (b) the armchair KYG/GR/KYG junction. The transport directions are the x and y directions, respectively. The supercell is sketched for (c) KYG and (d) strained graphene.

respectively, given as [50]

$$\begin{aligned} \text{Zigzag}: d_1 &= d_3 = a[1+(3-\upsilon)\varepsilon_Z/4], \\ d_2 &= a[1-\upsilon\varepsilon_Z], \\ \text{Armchair}: d_1 &= d_3 = a[1+(1-3\upsilon)\varepsilon_A/4], \\ d_2 &= a[1+\varepsilon_A], \end{aligned} \tag{9}$$

where ε_Z (ε_A) denotes the strength of the uniaxial strain. For graphene, $\upsilon = 0.165$ is Poisson's ratio [15]. If a shear strain is applied in the graphene region of AJs along zigzag or armchair direction, the deformed bond lengths are given as [51]

$$\begin{aligned} \text{Zigzag}: d_1 &= a\sqrt{1+\chi_1}, \quad d_2 = a\sqrt{1+\chi_2}, \\ d_3 &= a\sqrt{1+\chi_3}, \\ \text{Armchair}: d_1 &= a\sqrt{1+\chi_1/3}, \;\; d_2 = a, \\ d_3 &= a\sqrt{1+\chi_3/3}, \end{aligned} \tag{10}$$

where $\chi_1 = \varepsilon(\varepsilon - 2\sqrt{3})/4$, $\chi_2 = \varepsilon^2$, and $\chi_3 = \varepsilon(\varepsilon + 2\sqrt{3})/4$. We use $\gamma_Z = \varepsilon$ and $\gamma_A = \varepsilon/3$ to denote the strength of the shear strain along the zigzag and armchair directions, respectively.

The deformations will shift the positions of two valleys in momentum space, as shown in Fig. 3, the energy spectrum of the LCB of graphene. With the enlarged supercell shown in Fig. 2(d), two valleys are folded into the Γ point without strain, as shown in Fig. 3(a). When the uniaxial (shear) strain is applied in the graphene region of ZJs (AJs), two valleys are split along the k_x (k_y) direction, exactly the transport direction of ZJs (AJs), as shown in Figs. 3(b) and 3(c). Note that Fig. 3 only shows the energy spectrum of the LCB with the strains applied along the armchair direction; similar results can be obtained when the strains are applied along the zigzag direction.

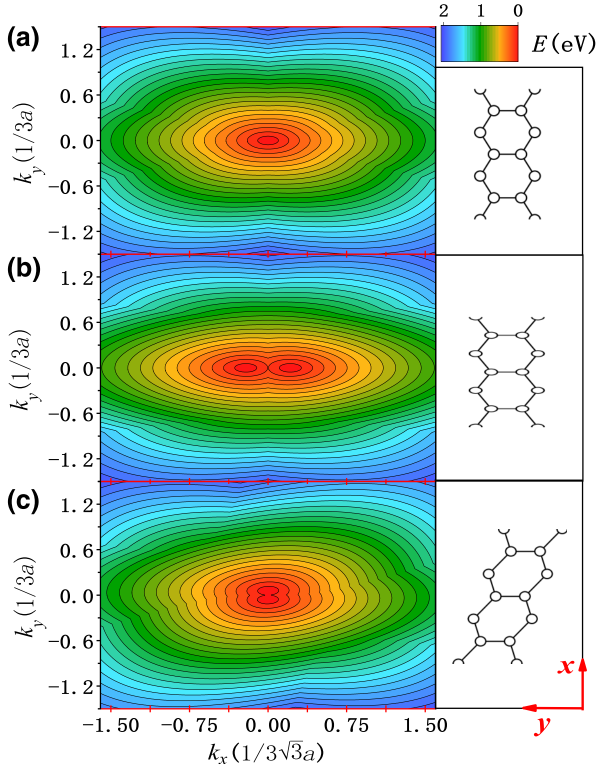

FIG. 3. The energy spectrum of the LCB of graphene (a) without strain, (b) under a uniaxial strain along the armchair direction with strain strength $\varepsilon_A = 2\%$, and (c) under a shear strain along the armchair direction with $\gamma_A = 2\%$. The supercells are sketched on the right-hand side.

The conductivities of ZJs and AJs under uniaxial or shear strain are shown in Fig. 4. Without losing generality, the lengths of the scattering regions $L_Z \approx L_A = 450a$ by setting $N_Z = 87$ and $N_A = 150$. Note that, under a first-order approximation, δk is proportional to the strain strength when the strain is applied to the graphene lattice along the armchair or zigzag direction, with the relation $\delta k = (1+\upsilon)\beta\varepsilon_{A(Z)}/2$ for uniaxial strain and $\delta k = \beta\gamma_{A(Z)}/2$ for shear strain [45]. In Fig. 4, all conductivity curves oscillate perfectly with the strain, and the periods satisfy perfectly the condition $\delta kL = \pi$, with L the length of the strained graphene region. This implies that the valley precession period is independent of the transverse wave vector. Moreover, the periods of the conductivity oscillations are also independent of the Fermi energy E_F of incident electrons. In all situations, the conductivity maxima can reach $2e^2/h$ and the conductivity minima are very close to zero. For the ZJ, the period of G in Fig. 4(a) is slightly smaller than that in Fig. 4(b). This is attributed to the small change of the length of graphene region under the strain. In the ZJ, the tensile strain along the zigzag direction

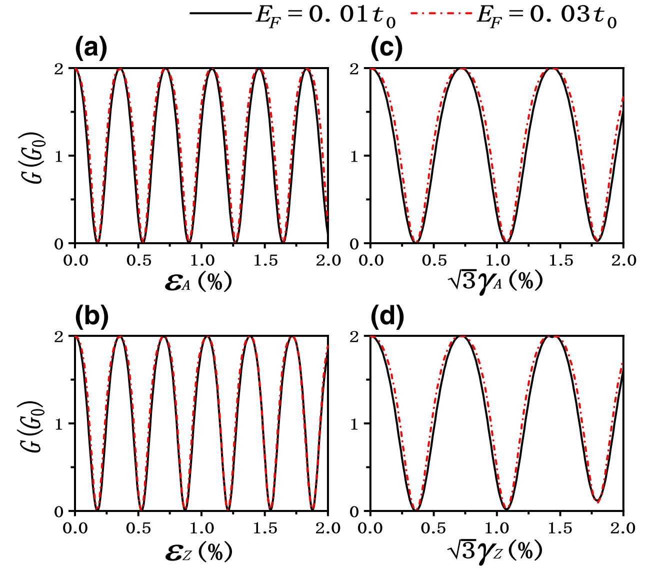

FIG. 4. The conductivities as functions of the strain strength for (a),(b) zigzag junctions and (c),(d) armchair junctions. The length of the scattering region $L_Z \approx L_A = 450a$ ($N_Z = 87, N_A = 150$) and the Fermi energies are chosen as $E_F = 0.01t_0$ and $E_F = 0.03t_0$. The uniaxial strain is applied in the graphene region of zigzag junctions along the (a) armchair and (b) zigzag direction. The shear strain is applied in the graphene region of armchair junctions along the (c) armchair and (d) zigzag direction. $U_A = 0.05t_0$ and the energy splitting between the LCB and the second conduction band is $2\Delta_0 = 2U_A/3$.

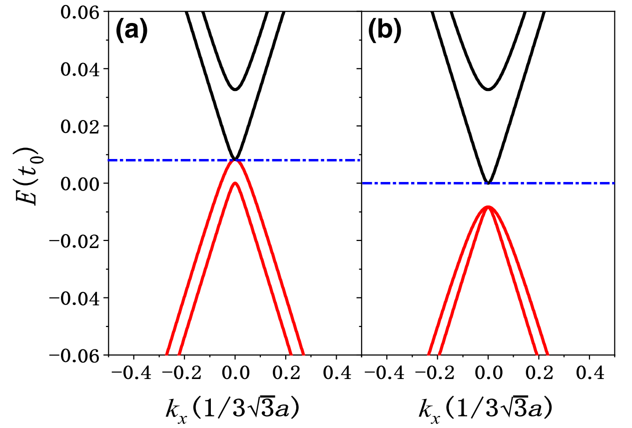

FIG. 5. The band structures of zigzag and armchair KYG. The parameters are set as $U_A = 0.05t_0$ and $\delta t = 0.05t_0$, with (a) $U_B = U_A/6$ and (b) $U_B = -U_A/6$. The blue dot-dashed lines show the bottoms of the LCBs. The transverse momenta are set as zero.

enhances the length, while the tensile strain along the armchair direction reduces the length. Figures 4(c) and 4(d) show the conductivities of the AJs under shear strain along the armchair and zigzag directions, respectively. Approximately, the period of G in Fig. 4(d) is the same as that in Fig. 4(c), which means that the conductivity of the AJ is independent of the direction of the applied shear strain. When γ_Z is around $1.75/\sqrt{3}\% \approx 1\%$, the minimum of G deviates from zero. This is attributed to the fact that a large shear deformation will also cause the movements of two valleys along the transverse momentum direction, i.e., the k_x direction [45].

B. $U_B \neq 0$ and $\delta t \neq 0$

When U_B and δt are considered in the KYG leads, according to Ref. [33], the low-energy effective Hamiltonian of KYG is given as

$$\begin{aligned} H^{\rm eff}_{\rm KYG}(\boldsymbol{k}) = {} & U_0\tau_0\sigma_0 + v_F\left(k_x\tau_0\sigma_x + k_y\tau_Z\sigma_y\right) \\ & + \Delta'\tau_0\sigma_z + \frac{\Delta}{2}\tau_x\left(\sigma_0+\sigma_z\right) \\ & + v_\delta\left(k_y\tau_x + k_x\tau_y\right)\sigma_y, \end{aligned} \tag{11}$$

where $U_0 = (\Delta + U_B)/2$, $\Delta' = (\Delta - U_B)/2$, $\Delta = 3U_At_0^2/(t_M + 2t_0)^2$, the modified Fermi velocity is $v_F = v_{F0}(2t_M + t_0)/(t_M + 2t_0)$, and $v_\delta = v_F(t_M - t_0)/(t_M + 2t_0)$ is the strength of valley-orbit interaction. When $\delta t \ll t_0$, the model can be approximately simplified as

$$\begin{aligned} H^{\rm eff}_{\rm KYG}(\boldsymbol{k}) = {} & v_{F0}\left(k_x\tau_0\sigma_x + k_y\tau_Z\sigma_y\right) \\ & + \frac{U_B}{2}\tau_0\left(\sigma_0 - \sigma_z\right) \\ & + \frac{\Delta_0}{2}\left(\tau_0+\tau_x\right)\left(\sigma_0+\sigma_z\right). \end{aligned} \tag{12}$$

Comparing with Eq. (2), the U_B term is added in Eq. (12). It is clearly seen that this term is valley degenerate and will not change the K-K' valley state of the LCB. Figures 5(a) and 5(b) show the band structures of KYG for $U_B > 0$ and $U_B < 0$, respectively. In both cases, $\delta t = 0.05t_0$. The energy spectrum is isotropic and the four eigenenergies at the Γ point are $E_{\rm KYG}(k_x = k_y = 0) = 0$, $2\Delta_0$, U_B (twofold degenerate). The bottom of the LCB moves from $E = 0$ to $E = U_B$ when $U_B > 0$, and remains at $E = 0$ when $U_B < 0$. The bottom of the second conduction band is pinned at $E = 2\Delta_0$. Thus, there is still an energy window $[U_B, 2\Delta_0]$ for $U_B > 0$ and $[0, 2\Delta_0]$ for $U_B < 0$, in which only the LCB is occupied. When the Fermi energy lies in this energy window, the incident electrons will be valley polarized with the valley K-K'.

The conductivities of zigzag and armchair KYG/GR/KYG junctions with various U_B and δt are shown in Fig. 6. The Fermi energy is set as $E_F = 0.03t_0$ with which the incident electrons are valley polarized to K-K'. The conductivities remain nearly the same for various U_B and δt and the periods of the conductivity oscillations are also the same as those in the case of $U_B = \delta t = 0$ shown in Figs. 4(a) and 4(c). The conductivity maxima also nearly reach $2e^2/h$ and the minima are close to zero. All these features verify that

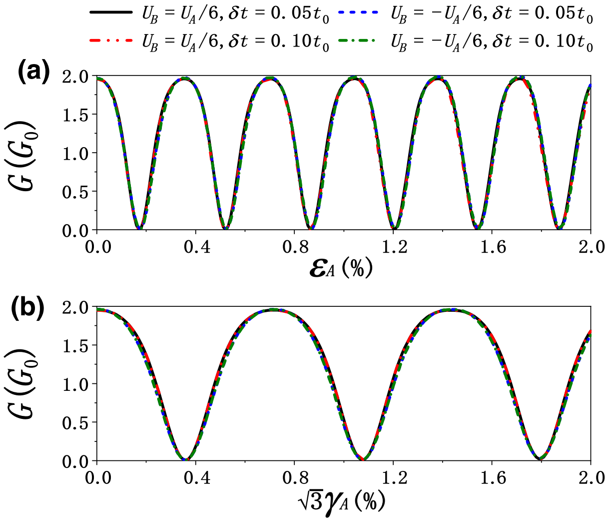

FIG. 6. The conductivity of (a) ZJs and (b) AJs. Uniaxial strain is applied to the ZJs and shear strain is applied to the AJs. Both strains are applied along the armchair direction, with the parameters set as: $L_Z \approx L_A = 450a$ ($N_Z = 87, N_A = 150$), $E_F = 0.03t_0$, $U_A = 0.05t_0$, $U_B = \pm U_A/6$, and $\delta t = 0.05t_0$ or $0.10t_0$.

U_B and δt have little effect on the valley precession and conductance oscillation of the junctions.

IV. CONCLUSION

In summary, we propose the realization of perfect valley precession and an ideal valley transistor in KYG/GR/KYG junctions. The valley precession and valley transistor are modulated by the strain in the GR region, which gives rise to an effective vector potential and separates two valleys in momentum space. It is notable that the spatial precession period is independent of both the Fermi energy and the transverse wave vector. This unique feature ensures an ideal valley transistor in which the conductivity perfectly oscillates with the applied strain. The conductivity maxima can reach $2e^2/h$ and the minima are close to zero, exhibiting a high on-to-off ratio. This finding provides a strategy to design ideal valleytronics and straintronics devices.

ACKNOWLEDGMENTS

The work described in this paper is supported by National Natural Science Foundation of China (NSFC, Grants No. 12174077 and No. 12174051) and National Natural Science Foundation of Guangdong Province (Grant No. 2021A1515012363).

[1] A. K. Geim, Graphene: status and prospects, Science **324,** 1530 (2009).

[2] A. K. Geim and K. S. Novoselov, The rise of graphene, Nat. Mater. **6**, 183 (2007).

[3] A. H. Castro Neto, F. Guinea, N. M. R. Peres, K. S. Novoselov, and A. K. Geim, The electronic properties of graphene, Rev. Mod. Phys. **81**, 109 (2009).

[4] D. R. Cooper, B. D'Anjou, N. Ghattamaneni, B. Harack, M. Hilke, A. Horth, N. Majlis, M. Massicotte, L. Vandsburger, E. Whiteway *et al.*, Experimental review of graphene, Int. Scholarly Res. Not. **2012**, 1 (2012).

[5] J. R. Schaibley, H. Yu, G. Clark, P. Rivera, J. S. Ross, K. L. Seyler, W. Yao, and X. Xu, Valleytronics in 2D materials, Nat. Rev. Mater. **1**, 1 (2016).

[6] S. A. Vitale, D. Nezich, J. O. Varghese, P. Kim, N. Gedik, P. Jarillo-Herrero, D. Xiao, and M. Rothschild, Valleytronics: Opportunities, challenges, and paths forward, Small **14,** 1801483 (2018).

[7] Y. Liu, Y. Gao, S. Zhang, J. He, J. Yu, and Z. Liu, Valleytronics in transition metal dichalcogenides materials, Nano Res. **12**, 2695 (2019).

[8] J. Xin, Y. Tang, Y. Liu, X. Zhao, H. Pan, and T. Zhu, Valleytronics in thermoelectric materials, Npj Quantum Mater. **3**, 1 (2018).

[9] D. Xiao, W. Yao, and Q. Niu, Valley-Contrasting Physics in Graphene: Magnetic Moment and Topological Transport, Phys. Rev. Lett. **99**, 236809 (2007).

[10] A. Cresti, B. K. Nikolić, J. H. García, and S. Roche, Charge, spin and valley Hall effects in disordered graphene, La Rivista del Nuovo Cimento **39**, 587 (2016).

[11] E. C. Marino, L. O. Nascimento, V. S. Alves, and C. M. Smith, Interaction induced quantum valley Hall effect in graphene, Phys. Rev. X **5**, 011040 (2015).

[12] F. Munoz, H. P. Ojeda Collado, G. Usaj, J. O. Sofo, and C. A. Balseiro, Bilayer graphene under pressure: Electron-hole symmetry breaking, valley Hall effect, and Landau levels, Phys. Rev. B **93**, 235443 (2016).

[13] M. Yamamoto, Y. Shimazaki, I. V. Borzenets, and S. Tarucha, Valley Hall effect in two-dimensional hexagonal lattices, valley Hall effect, and Landau levels, J. Phys. Soc. Jpn. **84**, 121006 (2015).

[14] F. Zhan, B. Zheng, X. Xiao, J. Fan, X. Wu, and R. Wang, Magnetic field induced valley-polarized quantum anomalous Hall effects in ferromagnetic van der Waals heterostructures, Phys. Rev. B **105**, 035131 (2022).

[15] F. Zhan, Z. Ning, L.-Y. Gan, B. Zheng, J. Fan, and R. Wang, Floquet valley-polarized quantum anomalous Hall state in nonmagnetic heterobilayers, Phys. Rev. B **105**, L081115 (2022).

[16] X. Chen, L. Zhang, and H. Guo, Valley caloritronics and its realization by graphene nanoribbons, Phys. Rev. B **92**, 155427 (2015).

[17] Z. Yu, F. Xu, and J. Wang, Valley Seebeck effect in gate tunable zigzag graphene nanoribbons, Carbon **99**, 451 (2016).

[18] L. Zhang, Z. Yu, F. Xu, and J. Wang, Influence of dephasing and B/N doping on valley Seebeck effect in zigzag graphene nanoribbons, Carbon **126**, 183 (2018).

[19] X. Zhai, S. Wang, and Y. Zhang, Valley-spin Seebeck effect in heavy group-IV monolayers, New J. Phys. **19**, 063007 (2017).

[20] A. Rycerz, J. Tworzydło, and C. Beenakker, Valley filter and valley valve in graphene, Nat. Phys. **3**, 172 (2007).

[21] T. Fujita, M. Jalil, and S. Tan, Valley filter in strain engineered graphene, Appl. Phys. Lett. **97**, 043508 (2010).

[22] D. Gunlycke and C. T. White, Graphene Valley Filter Using a Line Defect, Phys. Rev. Lett. **106**, 136806 (2011).

[23] A. Chaves, L. Covaci, K. Y. Rakhimov, G. A. Farias, and F. M. Peeters, Wave-packet dynamics and valley filter in strained graphene, Phys. Rev. B **82**, 205430 (2010).

[24] M.-K. Lee, N.-Y. Lue, C.-K. Wen, and G. Y. Wu, Valley-based field-effect transistors in graphene, Phys. Rev. B **86**, 165411 (2012).

[25] F. Qi, J. Cao, and G. Jin, Valley-controlled nonlocal transistor based on irradiated and biased bilayer graphene, Phys. Rev. B **98**, 045422 (2018).

[26] J. J. P. Thompson, D. J. Leech, and M. MuchaKruczyński, Valley-polarized tunneling currents in bilayer graphene tunneling transistors, Phys. Rev. B **99**, 085420 (2019).

[27] K. Chan, Valley dependent transport in graphene L junction, Phys. E (Amsterdam, Neth.) **99**, 160 (2018).

[28] C. Bao, H. Zhang, T. Zhang, X. Wu, L. Luo, S. Zho, Q. Li, Y. Hou, W. Yao, L. Liu *et al.*, Experimental Evidence of Chiral Symmetry Breaking in Kekulé-Ordered Graphene, Phys. Rev. Lett. **126**, 206804 (2021).

[29] C. Bao, H. Zhang, X. Wu, S. Zhou, Q. Li, P. Yu, J. Li, W. Duan, and S. Zhou, Coexistence of extended flat band and Kekulé order in Li-intercalated graphene, Phys. Rev. B **105**, L161106 (2022).

[30] C. Gutiérrez, C.-J. Kim, L. Brown, T. Schiros, D. Nordlund, E. B. Lochocki, K. M. Shen, J. Park, and A. N. Pasupathy, Imaging chiral symmetry breaking from Kekulé bond order in graphene, Nat. Phys. **12**, 950 (2016).

[31] V. Cheianov, V. Fal'ko, O. Syljuåsen, and B. Altshuler, Hidden Kekulé ordering of adatoms on graphene, Solid State Commun. **149**, 1499 (2009).

[32] G. Giovannetti, M. Capone, J. van den Brink, and C. Ortix, Kekulé textures, pseudospin-one Dirac cones, and quadratic band crossings in a graphene-hexagonal indium chalcogenide bilayer, Phys. Rev. B **91**, 121417(R) (2015).

[33] Y. Ren, X. Deng, Z. Qiao, C. Li, J. Jung, C. Zeng, Z. Zhang, and Q. Niu, Single-valley engineering in graphene superlattices, Phys. Rev. B **91**, 245415 (2015).

[34] J. W. F. Venderbos, M. Manzardo, D. V. Efremov, and J. van den Brink, Engineering interaction-induced topological insulators in a 3 × 3 substrate-induced honeycomb superlattice, Phys. Rev. B **93**, 045428 (2016).

[35] A. Pachoud, A. Ferreira, B. Özyilmaz, and A. H. Castro Neto, Scattering theory of spin-orbit active adatoms on graphene, Phys. Rev. B **90**, 035444 (2014).

[36] Q.-P. Wu, L.-L. Chang, Y.-Z. Li, Z.-F. Liu, and X.-B. Xiao, Electric-controlled valley pseudomagnetoresistance in graphene with Y-shaped Kekulé lattice distortion, Nanoscale Res. Lett. **15**, 1 (2020).

[37] O. Gamayun, V. Ostroukh, N. Gnezdilov, İ. Adagideli, and C. Beenakker, Valley-momentum locking in a graphene superlattice with Y-shaped Kekulé bond texture, New J. Phys. **20**, 023016 (2018).

[38] S. K. Wang and J. Wang, Valley precession in graphene superlattices, Phys. Rev. B **92**, 075419 (2015).

[39] J. J. Wang, S. Liu, J. Wang, and J.-F. Liu, Valley-coupled transport in graphene with Y-shaped Kekulé structure, Phys. Rev. B **98**, 195436 (2018).

[40] Q.-P. Wu, Z.-F. Liu, A.-X. Chen, X.-B. Xiao, H. Zhang, and G.-X. Miao, Valley precession and valley polarization in graphene with inter-valley coupling, J. Phys.: Condens. Matter **29**, 395303 (2017).

[41] S. Datta and B. Das, Electronic analog of the electro-optic modulator, Appl. Phys. Lett. **56**, 665 (1990).

[42] V. M. Pereira and A. H. Castro Neto, Strain Engineering of Graphene's Electronic Structure, Phys. Rev. Lett. **103**, 046801 (2009).

[43] F. Zhai, X. Zhao, K. Chang, and H. Q. Xu, Magnetic barrier on strained graphene: A possible valley filter, Phys. Rev. B **82**, 115442 (2010).

[44] L. Yang and J. Han, Electronic Structure of Deformed Carbon Nanotubes, Phys. Rev. Lett. **85**, 154 (2000).

[45] Y. Li, X. Jiang, Z. Liu, and Z. Liu, Strain effects in graphene and graphene nanoribbons: the underlying mechanism, Nano Res. **3**, 545 (2010).

[46] C. Si, Z. Sun, and F. Liu, Strain engineering of graphene: A review, Nanoscale **8**, 3207 (2016).

[47] C. W. Groth, M. Wimmer, A. R. Akhmerov, and X. Waintal, Kwant: A software package for quantum transport, New J. Phys. **16**, 063065 (2014).

[48] C. W. J. Beenakker, Specular Andreev Reflection in Graphene, Phys. Rev. Lett. **97**, 067007 (2006).

[49] P. E. Turchi, A. Gonis, and L. Colombo, Tight-Binding Approach to Computational Materials Science, Symposium Held December 1-3, 1997, Boston, Massachusetts, USA. Volume 491, Tech. Rep. (MATERIALS RESEARCH SOCIETY WARRENDALE PA, 1998).

[50] V. M. Pereira, A. H. Castro Neto, and N. M. R. Peres, Tight-binding approach to uniaxial strain in graphene, Phys. Rev. B **80**, 045401 (2009).

[51] N. Bandeira, D. da Costa, A. Chaves, G. Farias, and R. Costa Filho, Gap opening in graphene nanoribbons by application of simple shear strain and in-plane electric field, J. Phys.: Condens. Matter **33**, 065503 (2020).